A Wavelet-based method for multifractal analysis of rough surfaces : Applications to high-resolution satellite images of cloud structure

A. Arneodo*, S. G. Roux† and N. Decoster**

*Centre de Recherche Paul Pascal, Avenue Schweitzer, 33600 Pessac, France.
†Laboratoire de Physique, CNRS UMR 5672, École Normale Supérieure de Lyon, 46 allée d'Italie, 69364 Lyon Cedex 07, France.
**Noveltis, 2 Avenue de l'Europe, 31520 Ramonville Saint Agne, France.

Abstract. We apply the 2D wavelet transform modulus maxima (WTMM) method to high-resolution LANDSAT satellite images of cloudy scenes. The computation of the $\tau(q)$ and $D(h)$ multifractal spectra of the radiance fields confirms the relevance of the multifractal description to account for the intermittent nature of marine stratocumulus clouds. This analysis reveals that with the available set of experimental data, there is no way to discriminate between various phenomenological cascade models recently proposed to account for intermittency and their log-normal approximations. We emphasize the log-normal random $\mathcal{W}$-cascade model on separable wavelet orthogonal basis introduced in (N. Decoster, S.G. Roux, A.Arneodo, Eur. Phys. J. B **15**, 739(2000)), as a very attractive model (at least as compared to the models commonly used in the literature) of the cloud architecture. Finally, we comment on the multifractal properties of marine stratocumulus radiance fields comparatively to previous experimental analysis of velocity and temperature fluctuations in high Reynolds number turbulence.

INTRODUCTION

The problematic of nonlinear variability over a wide range of scales has been considered for a long time with respect to the highly intermittent nature of turbulent flows in fluid dynamics [1, 2]. Special attention has been paid to their asymptotic and possibly universal behavior when the dissipation length goes to zero, *i.e.*, when the Reynolds number goes to infinity. Besides wind-tunnel and laboratory (grid, jet, ...) experiments, the atmosphere is a huge natural laboratory where high Reynolds number (fully developed) turbulent dynamics can be studied. Clouds, which are at the source of the hydrological cycle, are the most obvious manifestation of the earth's turbulent atmospheric dynamics [3, 4]. By modulating the input of solar radiation, they play a critical role in the maintenance of the earth's climate [5]. They are also one of the main sources of uncertainty in current climate modeling [6]. During many years, the lack of data hindered our understanding of cloud microphysics and cloud-radiation interactions. Until quite recently, the internal structure of clouds was probed by balloons or aircrafts that penetrated the cloud layer, revealing an extreme variability of 1D cuts of some cloud fields, *e.g.* liquid water content (LWC) [7, 8]. Indeed, during the past fifteen years, vast amounts of data on the distribution of atmospheric liquid water from a variety of sources were collected and analyzed in many different ways. All these data contain information on spatial and/or temporal cor-

relations in cloudiness, enabling the investigation of scale invariance over a range from a few centimeters to hundred of kilometers. An attractive alternative to *in situ* probing is to use high-resolution satellite imagery that now provides direct information about the fluctuations in liquid water concentration in the depths of clouds [9, 10, 11, 12, 13, 14, 15]. These rather sophisticated remote sensing systems called "millimeter radars" are actually sensitive not only to precipating rain drops but also to suspended cloud droplets. Spectral analysis of the recorded 2D radiance field [12, 13, 14, 15] confirms previous 1D findings that make it likely that cloud scenes display scaling over a wide range of scales.

Fractal analysis of atmospheric data has gained considerable momentum since Lovejoy's seminal paper [3] on the area-perimeter relation for clouds and rain. Since then, such morphological studies have become rather popular, following a path open by Mandelbrot in his famous books [16]. Starting from the middle eighties, high-resolution cloud liquid water data became available, confirming the fractal nature of the cloud structure. Most preliminary analysis of these complex 1D signals focused on the characterization of scale invariance in Fourier space [7, 8, 9, 10, 11, 12, 13, 14, 15]. In particular, the fluctuations of liquid water density in clouds were shown to have power-law energy spectra, $S(k) \sim 1/k^\beta$, over a large range of scales, from tens of meters to tens of kilometers. Let us point out that the estimated spectral exponent $\beta \sim 1.4 - 1.7$, is close to the prediction $\beta = 5/3$ of Corssin [17]-Obukhov [18] phenomenology for a passive scalar in fully developed 3D turbulence as well as to Kraichnan [19] prediction for 2D turbulence. But as discussed in Ref. [20], power-spectral analysis has been heavily criticized for its intrinsic inability to capture multifractal scaling. From the measurement of the spectral exponent $\beta = 2H + 1$, one gets some estimate of the so-called Hurst exponent, $H \sim 0.20 - 0.35$, from which one learns that the fluctuating field is singular and non stationary ($0 < H < 1$). Unfortunately, the intermittent nature of the recorded liquid water data required new concepts and more elaborated technical tools. Again, one has to give credit to Lovejoy and co-workers [21, 22, 23, 24, 25] for applying the multifractal description to atmospheric phenomena. Using the trace moment and double trace moment techniques, they have brought experimental evidence for multiple scaling (or in other words, the existence of a continuum of scaling exponent values) in various geophysical fields. More recently, Davis and co-workers [8, 26] have used the structure function method to study LWC data recorded during ASTEX and FIRE programs. Both these analyses converge to the conclusion that the internal marine stratocumulus (Sc) structure is multifractal over at least three decades in scales. Quite similar multifractal behavior has been reported by Wiscombe *et al* [27] when analazing liquid water path (LWP) data (*i.e.*, column integrated LWC), from the Atmosperic Radiation Measurement (ARM) archive. Even though all these studies seem to agree, at least as far as their common diagnostic of multifractal scaling of the cloud structure, they all concern 1D data. To our knowledge, the stucture function method has been also applied to 1D cuts of high-resolution satelitte images [15], but we are not aware of any result coming out from a specific 2D analysis.

In this paper, our first goal is to take advantage of the 2D wavelet transform modulus maxima (WTMM) method introduced in Ref. [20] and further tested on synthetic multifractal surfaces in Ref. [28], to carry out a multifractal analysis of high-resolution satelitte images of Sc cloudy scenes [29, 30, 31]. Our objective is not only to extend

previous analysis of 1D profiles to full 2D image processing, but also to remedy to the insufficiencies of the structure function method which, as pointed out in Ref. [32], fails to achieve complete multifractal characterization. The 2D WTMM method is likely to provide reliable quantitative estimates of the entire $\tau(q)$ and $D(h)$ multifractal spectra, within the perspective of confirming the intermittent nature of the internal cloud structure. Although this result would not be a surprise in such a highly turbulent environment, the possibility of comparing quantitatively the statistical scaling properties of the optical depth or the radiance fields with those of the velocity or temperature fluctuations in high Reynolds turbulent flows, might be very instructive as far as the influence of atmospheric dynamics on the liquid water distribution in clouds.

A MULTIFRACTAL FORMALISM BASED ON THE 2D WAVELET TRANSFORM

Analyzing wavelets for multi-scale edge detection

In recent years, there has been increasing interest in the application of the continuous wavelet transform to image processing [33, 34]. The edges of the different structures that appear in an image are often the most important features for pattern recognition. Hence, in computer vision [35], a large class of edge detectors look for points where the gradient of the image intensity has a modulus which is locally maximum in its direction. As originally noticed by Mallat and collaborators [36, 37], with an appropriate choice of the analyzing wavelet, one can reformalize the Canny's multi-scale edge detector [38] in terms of a 2D wavelet transform. The general idea is to start by smoothing the discrete image data by convolving it with a filter and then to compute the gradient on the smoothed signal.

Let us consider two wavelets that are, respectively, the partial derivative with respect to x and y of a 2D smoothing function $\phi(x,y)$:

$$\psi_1(x,y) = \frac{\partial \phi(x,y)}{\partial x} \text{ and } \psi_2(x,y) = \frac{\partial \phi(x,y)}{\partial y} \ . \tag{1}$$

We will assume that ϕ is a well localized (around $x = y = 0$) isotropic function that depends on $|\mathbf{x}|$ only. In this work, we will mainly use the gaussian function:

$$\phi(x,y) = e^{-(x^2+y^2)/2} = e^{-|\mathbf{x}|^2/2} \ , \tag{2}$$

as well as the isotropic mexican hat:

$$\phi(\mathbf{x}) = (2 - \mathbf{x}^2)e^{-|\mathbf{x}|^2/2} \ . \tag{3}$$

The corresponding analyzing wavelets ψ_1 and ψ_2 are illustrated in Figure 1. They have one and three vanishing moments when using respectively the gaussian function and the mexican hat as smoothing function.
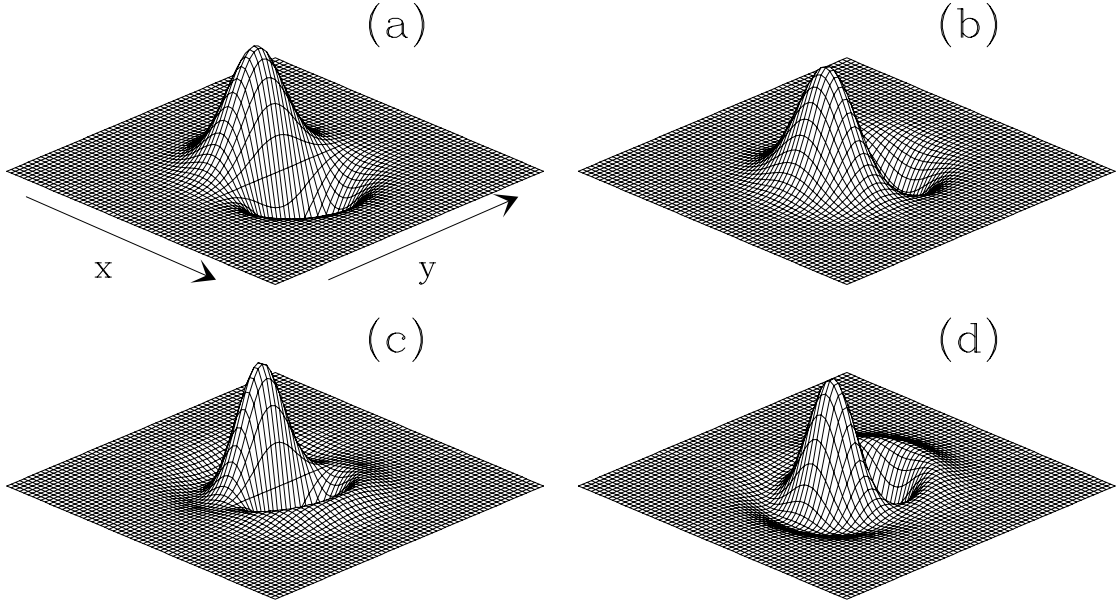
FIGURE 1. The analyzing wavelets ψ_1 and ψ_2 defined in equation (1). First-order analyzing wavelets obtained from a gaussian smoothing function ϕ (Eq. (2)): (a) ψ_1; (b) ψ_2. Third-order analyzing wavelets obtained from the isotropic mexican hat smoothing function ϕ (Eq. (3)): (c) ψ_1; (d) ψ_2.

For any function $f(x,y) \in L^2(\mathbb{R})$, the wavelet transform with respect to ψ_1 and ψ_2 can be expressed in a vectorial form:

$$\mathbf{T}_{\boldsymbol{\psi}}[f](\mathbf{b},a) = \left\{ \begin{array}{l} T_{\psi_1}[f] = a^{-2} \int d^2\mathbf{x} \, \psi_1\big(a^{-1}(\mathbf{x}-\mathbf{b})\big) f(\mathbf{x}) \\ T_{\psi_2}[f] = a^{-2} \int d^2\mathbf{x} \, \psi_2\big(a^{-1}(\mathbf{x}-\mathbf{b})\big) f(\mathbf{x}) \end{array} \right\} \tag{4}$$

Then, after a straightforward integration by parts, one gets:

$$\begin{aligned} \mathbf{T}_{\boldsymbol{\psi}}[f](\mathbf{b},a) &= a^{-2} \boldsymbol{\nabla} \left\{ \int d^2\mathbf{x} \, \phi\big(a^{-1}(\mathbf{x}-\mathbf{b})\big) f(\mathbf{x}) \right\}, \\ &= \boldsymbol{\nabla} \big\{ T_\phi[f](\mathbf{b},a) \big\}, \\ &= \boldsymbol{\nabla} \big\{ \phi_{\mathbf{b},a} * f \big\}. \end{aligned} \tag{5}$$

If $\phi(\mathbf{x})$ is simply a smoothing filter like the Gaussian function (Eq. (2)), then equation (5) amounts to define the 2D wavelet transform as the gradient vector of $f(\mathbf{x})$ smoothed by dilated versions $\phi(a^{-1}\mathbf{x})$ of this filter.

In the following, we will mainly use the representation involving the modulus and the argument of the wavelet transform:

$$\mathbf{T}_{\boldsymbol{\psi}}[f](\mathbf{b},a) = \big(\mathcal{M}_{\boldsymbol{\psi}}[f](\mathbf{b},a), \mathcal{A}_{\boldsymbol{\psi}}[f](\mathbf{b},a) \big), \tag{6}$$

with

$$\mathcal{M}_\psi[f](\mathbf{b},a) = \left|\mathbf{T}_\psi[f](\mathbf{b},a)\right|,$$
$$= \left[\left(T_{\psi_1}[f](\mathbf{b},a)\right)^2 + \left(T_{\psi_2}[f](\mathbf{b},a)\right)^2\right]^{1/2} \tag{7}$$

and

$$\mathcal{A}_\psi[f](\mathbf{b},a) = \mathrm{Arg}\left(T_{\psi_1}[f](\mathbf{b},a) + iT_{\psi_2}[f](\mathbf{b},a)\right). \tag{8}$$

Singularity detection and processing with the wavelet transform modulus maxima

The multifractal formalism accounts for possible fluctuations of the local regularity of a rough surface as defined by the Hölder (local roughness) exponent $h(\mathbf{x})$ of the function $f(\mathbf{x})$ whose graph defines the rough surface under study [20] :

$$f(\mathbf{x}+\mathbf{l}) - f(\mathbf{x}) \sim |\mathbf{l}|^{h(\mathbf{x})}, \tag{9}$$

for $|\mathbf{l}| \to 0$ (we refer the reader to Ref. [20] for a more rigorous definition of the Hölder exponent). The so-called $D(h)$ singularity spectrum is defined as the Haussdorf dimension of the set of points $\mathbf{x}$ where the local roughness exponent $h(\mathbf{x})$ is h. As pointed out in Ref. [20], a very efficient way to perform point-wise regularity analysis is to use the wavelet transform modulus maxima.

In the spirit of Canny edge detection [38], at a given scale a, the wavelet transform modulus maxima (WTMM) are defined as the points $\mathbf{b}$ where the wavelet transform modulus $\mathcal{M}_\psi[f](\mathbf{b},a)$ (Eq. (7)) is locally maximum along the gradient direction given by the wavelet transform argument $\mathcal{A}_\psi[f](\mathbf{b},a)$ (Eq. (8)). These modulus maxima are inflection points of $f * \phi_a(\mathbf{x})$. As illustrated in Figure 2, these WTMM lie on connected chains hereafter called *maxima chains* [20, 29, 30]. In theory, one only needs to record the position of the local maxima of $\mathcal{M}_\psi$ along the maxima chains together with the value of $\mathcal{M}_\psi[f]$ and $\mathcal{A}_\psi[f]$ at the corresponding locations. At each scale a, our wavelet analysis thus reduces to store those WTMM maxima (WTMMM) only. They indicate locally the direction where the signal has the sharpest variation. This orientation component is the main difference between 1D and 2D wavelet transform analysis. These WTMMM are disposed along connected curves across scales called *maxima lines* [20, 28, 30]. We will define the WT skeleton as the set of maxima lines that converge to the (x,y)-plane in the limit $a \to 0^+$. This WT skeleton is likely to contain all the information concerning the local Hölder regularity properties of the function f under consideration. Indeed one can prove [20] that, provided the first n_ψ moments of ψ are zero, then :

$$\mathcal{M}_\psi[f]\left(\mathcal{L}_\mathbf{x}(a)\right) \sim a^{h(\mathbf{x})}, \tag{10}$$

along a maxima line pointing to the point $\mathbf{x}$ in the limit $a \to 0^+$, where $h(\mathbf{x})$ $(< n_\psi)$ is the local Hölder exponent of f. Moreover, along this maxima line, the wavelet transform

argument evolves towards the value :

$$\mathcal{A}_\psi[f]\big(\mathcal{L}_\mathbf{x}(a)\big) = \pi + \theta_\mathbf{x} \,, \tag{11}$$

in the limit $a \to 0^+$, where $\theta_\mathbf{x}$ is nothing but the direction of the largest variation of f around $\mathbf{x}$, *i.e.* the direction to follow from $\mathbf{x}$ to cross the maxima line at a given (small) scale. From the maxima line $\mathcal{L}_\mathbf{x}(a)$, one thus gets the required amplitude as well as directional informations to characterize the local Hölder regularity of f at $\mathbf{x}$.

The 2D wavelet transform modulus maxima method

The WTMM method consists in defining the following partitions functions directly from the WTMMM that belong to the wavelet transform skeleton [20]:

$$\mathcal{Z}(q,a) = \sum_{\mathcal{L} \in \mathcal{L}(a)} \left(\sup_{(\mathbf{x},a') \in \mathcal{L}, a' \leq a} \mathcal{M}_\psi[f](\mathbf{x},a') \right)^q \,, \tag{12}$$

where $q \in \mathbb{R}$. As compared to classical box-counting techniques [39, 40], the analyzing wavelet ψ plays the role of a generalized "oscillating box", the scale a defines its size, while the WTMM skeleton indicates how to position our oscillating boxes to obtain a partition (of $S = \cup S_h$) at the considered scale. Without the "sup" in equation (12), one would have implicitly considered a uniform covering with wavelets of the same size a. As emphasized in Refs [41, 42, 43], the "sup" can be regarded as a way of defining a "Hausdorff like" scale-adaptative partition which will prevent divergencies to show up in the calculation of $\mathcal{Z}(q,a)$ for $q < 0$.

Now, from the deep analogy that links the multifractal formalism to thermodynamics [42, 43], one can define the exponent $\tau(q)$ from the power-law behavior of the partition function:

$$\mathcal{Z}(q,a) \sim a^{\tau(q)} \,, \, a \to 0^+ \,, \tag{13}$$

where q and $\tau(q)$ play respectively the role of the inverse temperature and the free energy. The main result of the wavelet-based multifractal formalism is that in place of the energy and the entropy (*i.e.*, the variables conjugated to q and τ), one has the Hölder exponent h (Eq. (9)) and the singularity spectrum $D(h)$. This means that the $D(h)$ singularity spectrum of f can be determined from the Legendre transform of the partition function scaling exponent $\tau(q)$:

$$D(h) = \min_q \big(qh - \tau(q)\big) \,. \tag{14}$$

From the properties of the Legendre transform, it is easy to convince oneself that *homogeneous* (monofractal) fractal functions that involve singularities of unique Hölder exponent $h = \partial\tau/\partial q$, are characterized by a $\tau(q)$ spectrum which is a *linear* function of q. On the contrary, a *nonlinear* $\tau(q)$ curve is the signature of nonhomogeneous functions that display *multifractal* properties, in the sense that the Hölder exponent $h(\mathbf{x})$ is a

fluctuating quantity that depends upon the spatial position $\mathbf{x}$ (in other words the local roughness exponent is fluctuating from point to point). Let us note that the scaling exponent $\tau(q)$ has well-known meaning for some specific values of q : (i) $-\tau(0)$ is the fractal dimension of the set of singularities of f; (ii) $\tau(1)$ is related to the fractal dimension of the rough surface $\mathcal{S}$ $(z = f(x,y))$: $d_f(\mathcal{S}) = \max\big(2, 1 - \tau(1)\big)$; (iii) $\tau(2)$ is related to the scaling exponent β of the spectral density $S(\mathbf{k}) = |\hat{f}(\mathbf{k})|^2 \sim |\mathbf{k}|^\beta$ with $\beta = 4 - \tau(2)$.

TEST APPLICATIONS OF THE 2D WTMM METHOD TO SYNTHETIC ROUGH SURFACES

Isotropic fractional Brownian surfaces

Since its introduction by Mandelbrot and Van Ness [44], the fractional Brownian motion (fBm) has become a very popular model in signal and image processing [16, 45]. In one dimension, fBm has proved useful for modeling various physical phenomena with long-range dependence, *e.g.*, "$1/f$" noises. The generalization of Brownian motion to more than one dimension was first considered by Levy [46]. The generalization of fBm follows along similar lines. A 2D fBm $B_H(\mathbf{x})$ indexed by $H \in]0,1[$, is a process with stationary zero-mean Gaussian increments that can be used to generate random self-affine surfaces with known statistical properties :

$$\tau(q) = qH - 2 \,. \tag{15}$$

By Legendre transforming $\tau(q)$ according to equation (14), one gets the following expression for the singularity spectrum :

$$\begin{aligned} D(h) \ &= 2 \qquad \text{if } h = H \,, \\ &= -\infty \quad \text{if } h \neq H \,. \end{aligned} \tag{16}$$

Thus fBm surfaces are the representation of homogeneous stochastic monofractal functions characterized by a singularity spectrum which reduces to a single point.

We have tested the 2D WTMM method described in the previous section, on 32 realizations of a 2D fBm process with $H = 1/3$. We have wavelet transformed 32 (1024×1024) images of $B_{H=1/3}$ with an isotropic first-order analyzing wavelet. To master edge effects, we then restrain our analysis to the 512×512 central part of the wavelet transform of each image. In Figure 2 is illustrated the computation of the maxima chains and the WTMMM for an individual image at three different scales. In Figure 2b is shown the convolution of the original image (Fig. 2a) with the isotropic gaussian smoothing filter ϕ (Eq. (2)). According to the definition of the wavelet transform modulus maxima, the maxima chains correspond to well defined edge curves of the smoothed image. The local maxima of $\mathcal{M}_\psi$ along these curves are located at the points where the sharpest intensity variation is observed. The corresponding arrows clearly indicate that locally, the gradient vector points in the direction (as given by $\mathcal{A}_\psi$) of maximum change of the intensity surface. When going from large scale (Fig. 2d) to small scale (Fig. 2c), the characteristic average distance between two nearest neighbour WTMMM decreases
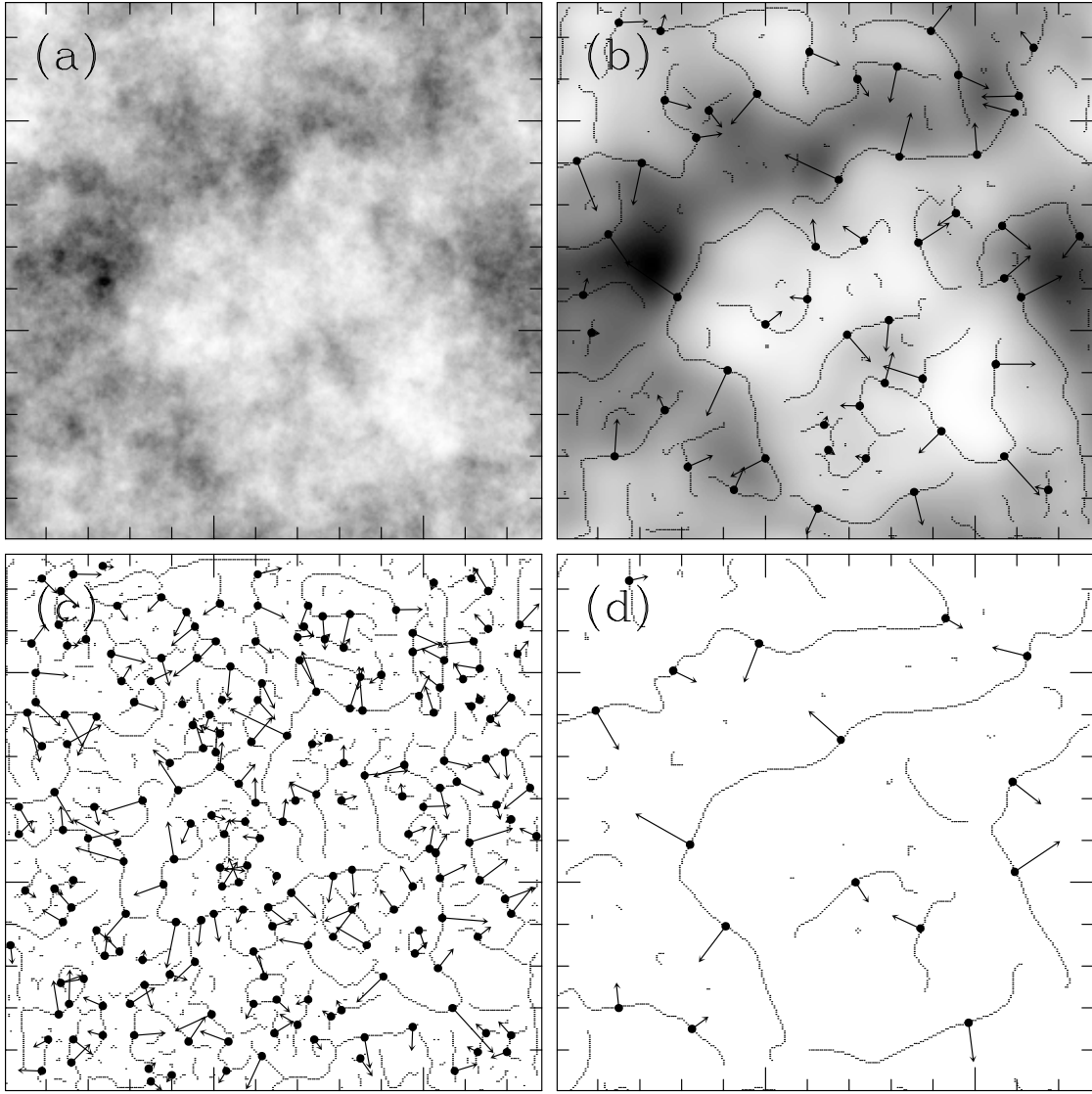
FIGURE 2. 2D wavelet transform analysis of $B_{H=1/3}(\mathbf{x})$. ψ is a first-order radially symmetric analyzing function (see Fig. 1). (a) 32 grey-scale coding of the central 512×512 portion of the original image. In (b) $a = 2\sigma_W$, (c) $a = 2^{0.1}\sigma_W$ and (d) $a = 2^{1.9}\sigma_W$, are shown the maxima chains; the local maxima of $\mathcal{M}_\psi$ along these chains are indicated by ($\bullet$) from which originate an arrow whose length is proportional to $\mathcal{M}_\psi$ and its direction (with respect to the x-axis) is given by $\mathcal{A}_\psi$. In (b), the smoothed image $\phi_{\mathbf{b},a} * B_{1/3}$ (Eq. (5)) is shown as a grey-scale coded background from white (min) to black (max). $\sigma_W = 13$ (pixels) is the characteristic size of ψ at the smallest resolved scale.

like a. This means that the number of WTMMM and in turns, the number of maxima lines, proliferates across scales like a^{-2}. The corresponding wavelet transform skeleton is shown in Figure 3. As confirmed just below, when extrapolating the arborescent structure of this skeleton to the limit $a \to 0^+$, one recovers the theoretical result that the support of the singularities of a 2D fBm has a dimension $d_F = 2$, *i.e.*, $B_{H=1/3}(\mathbf{x})$ is nowhere differentiable [16, 45, 46].
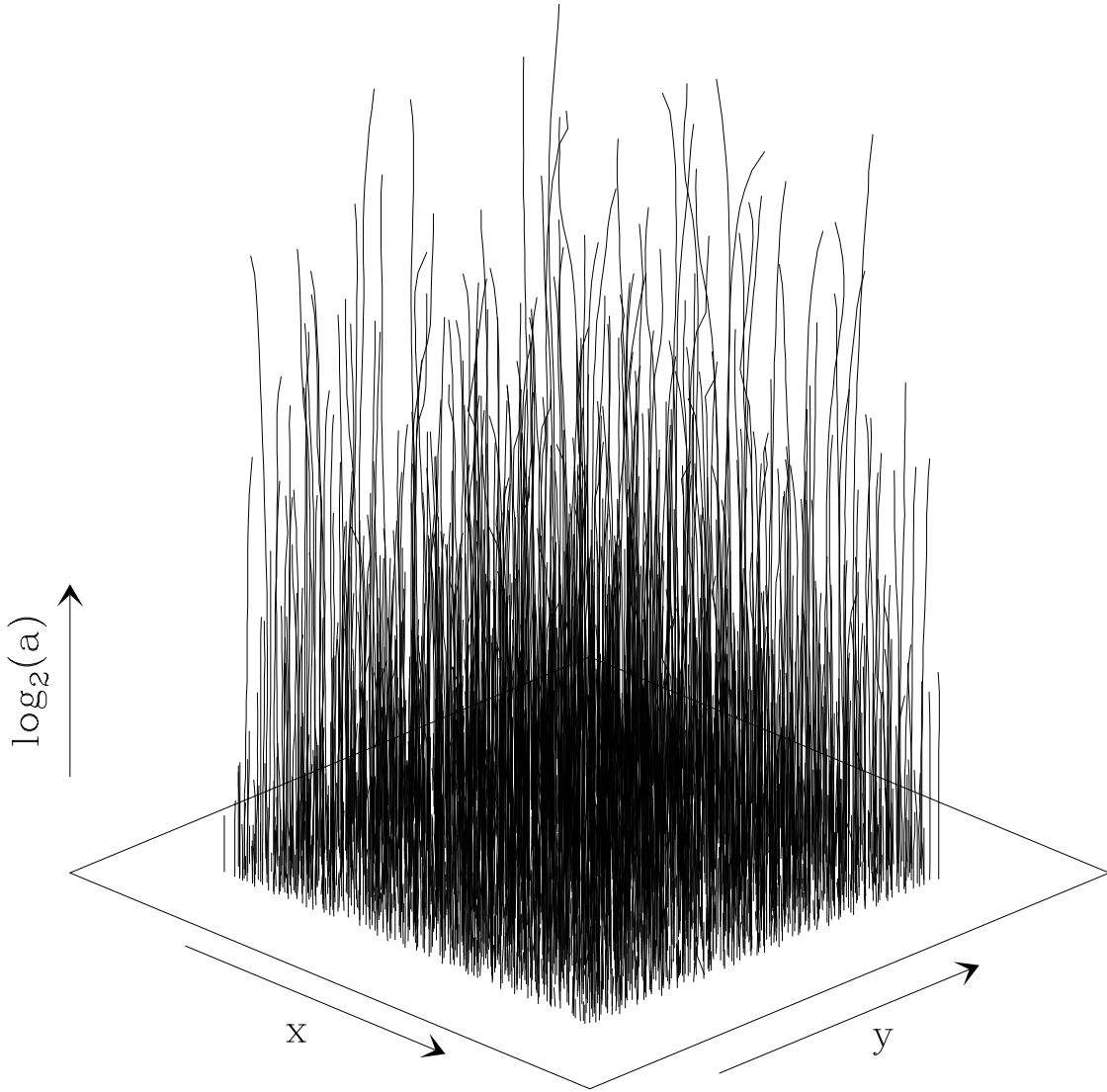
FIGURE 3. Wavelet transform skeleton of the 2D fBm image shown in Figure 2a. This skeleton is defined by the set of maxima lines obtained after linking the WTMMM detected at different scales. Same analyzing wavelet as in Figure 2.

In Figure 4 are reported the results of the computation of the $\tau(q)$ and $D(h)$ spectra using the 2D WTMM method. As shown in Figure 4a, the average partition function $\mathcal{Z}(q,a)$ (over 32 images of $B_{1/3}(\mathbf{x})$) displays a remarkable scaling behavior over more than 3 octaves when plotted *versus* a in a logarithmic representation (Eqs. (12) and (13)). Moreover, for a wide range of values of $q \in [-4, 6]$, the data are in good agreement with the theoretical $\tau(q)$ spectrum (Eq. (15)). When proceeding to a linear regression fit of the data over the first two octaves, one gets the $\tau(q)$ spectra shown in Figure 4b for three values of the fBm index $H = 1/3$, $1/2$ and $2/3$. Whatever H, the data systematically fall on a straight line, the signature of homogeneous (monofractal) scaling properties. In Figure 4c are reported the corresponding estimates of $D(h)$, from Legendre transforming
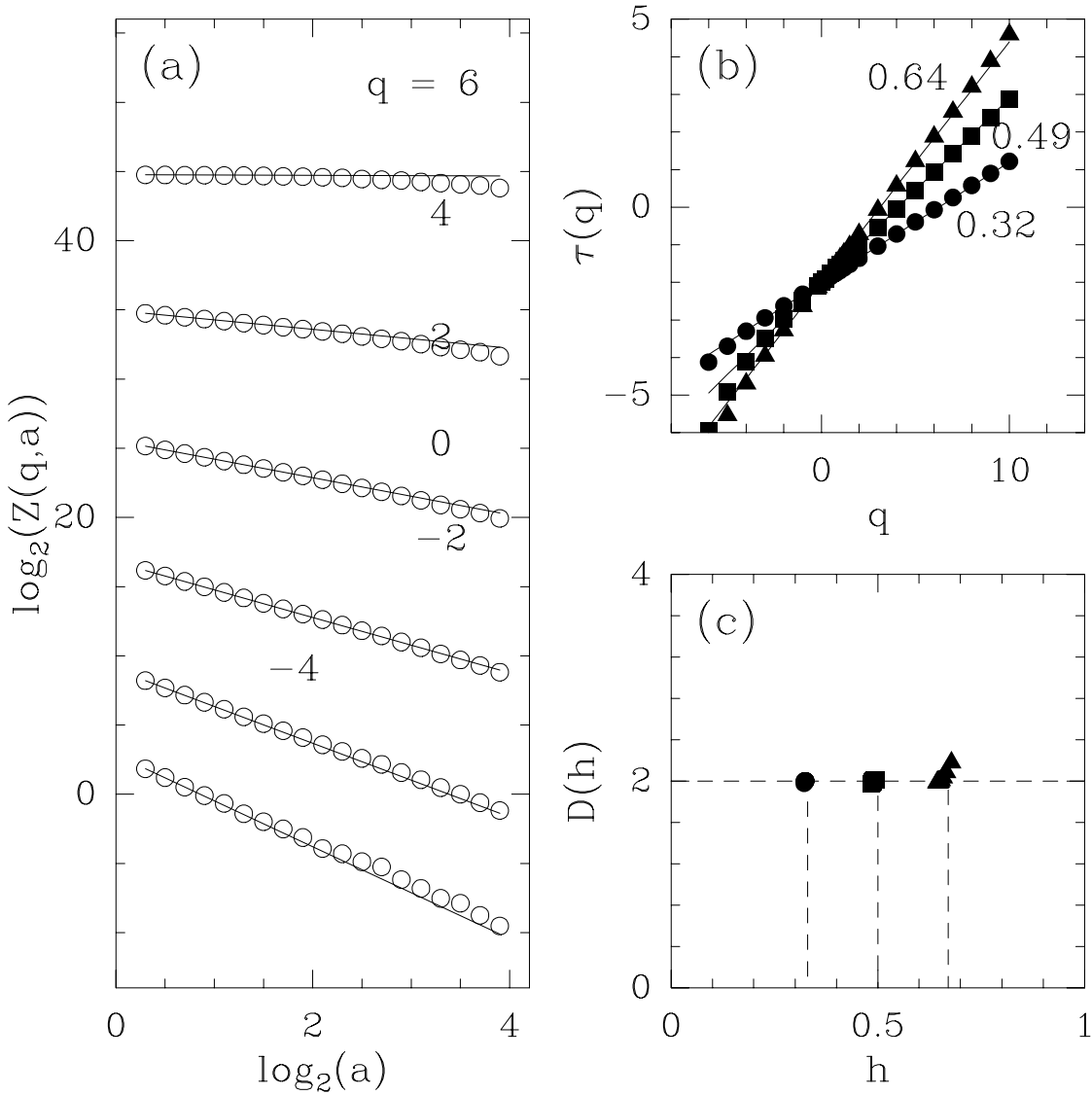
FIGURE 4. Determination of the $\tau(q)$ and $D(h)$ spectra of 2D fBm with the 2D WTMM method [20]. (a) $\log_2 \mathcal{Z}(q,a)$ *vs* $\log_2 a$; the solid lines correspond to the theoretical predictions $\tau(q) = qH - 2$ (Eq. (15)) with $H = 1/3$. (b) $\tau(q)$ *vs* q for $H = 1/3$ (●), $1/2$ (■) and $2/3$ (▲); the solid lines correspond to linear regression fit estimates of H. (c) $D(h)$ *vs* h. Same analyzing wavelet as in Figure 2. These results correspond to averaging over 32 (1024×1024) fBm images. a is expressed in σ_W units.

the $\tau(q)$ data (Eq. (14)). The results obtained for both the $\tau(q)$ and $D(h)$ spectra are thus in remarkable agreement with the theoretical predictions given by equations (15) and (16) respectively. The 2D WTMM method can thus be considered as having successfully passed the test of homogeneous fBm rough surfaces.

When further investigating the joint probability distribution function $P_a(\mathcal{M}, \mathcal{A})$ as computed from the wavelet transform skeleton of 32 (1024×1024) images of $B_{1/3}(\mathbf{x})$, one can check that this pdf actually factorizes $P_a(\mathcal{M}, \mathcal{A}) = P_a(\mathcal{M}) P_a(\mathcal{A})$, where $P_a(\mathcal{M}) = \int d\mathcal{A}\, P_a(\mathcal{M}, \mathcal{A})$ and $P_a(\mathcal{A}) = \int d\mathcal{M}\, P_a(\mathcal{M}, \mathcal{A})$ are shown in Figure 5 for
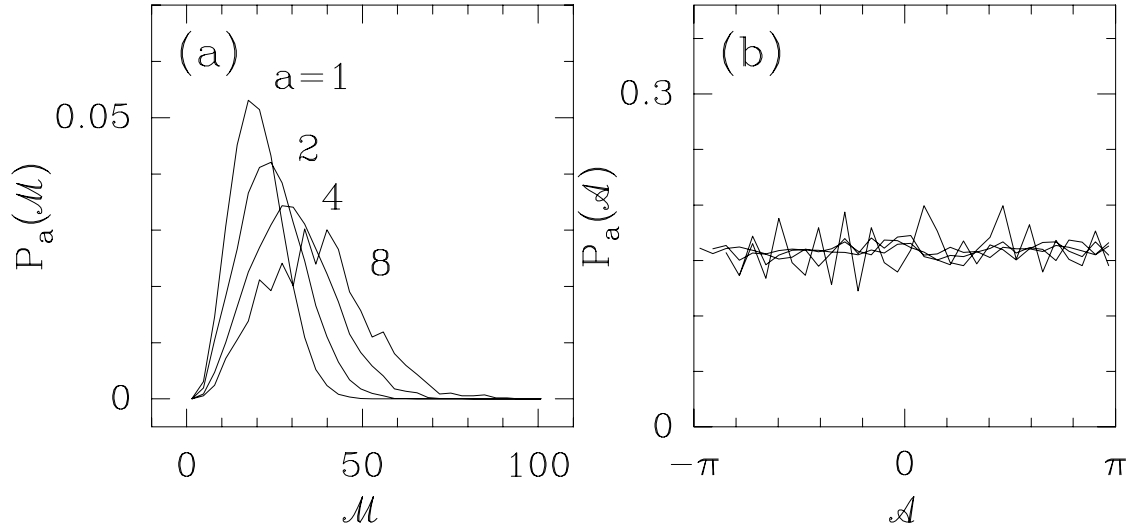
FIGURE 5. Pdf's of the WTMMM coefficients of $B_{1/3}(\mathbf{x})$ as computed at different scales $a = 1, 2, 4$ and 8 (in σ_W units). (a) $P_a(\mathcal{M})$ *vs* $\mathcal{M}$. (b) $P_a(\mathcal{A})$ *vs* $\mathcal{A}$. ψ is the first-order analyzing wavelet shown in Figure 1. These results correspond to averaging over 32 (1024×1024) fBm images.

four different values of the scale parameter. This factorization means that the scale-invariance properties are statistically independent of the angular information contained in $P_a(\mathcal{A})$. As seen in Figure 5a, $P_a(\mathcal{M})$ decreases fast to zero at zero. This explains that when concentrating on the wavelet transform skeleton, the integral in the r.h.s. of equation (12) does not diverge when considering negative q values. This remark is at the heart of the 2D WTMM method; by allowing us to compute the $\tau(q)$ spectrum for negative as well as positive q values, the 2D WTMM method is a definite step beyond the 2D structure function method which is intrinsically restricted to positive q values. The corresponding pdf's $P_a(\mathcal{A})$ are represented in Figure 5b. $P_a(\mathcal{A})$ clearly does not evolve across scales. Moreover, except some small amplitude fluctuations observed at the largest scale, $P_a(\mathcal{A}) = 1/2\pi$ is a flat distribution as expected for statistically isotropic scale-invariant rough surfaces.

Isotropic multifractal synthetic rough surfaces

In Figure 6 is illustrated the computation of the maxima chains and the WTMMM for an individual image of a multifractal rough surface generated with the log-normal $\mathcal{W}$-cascade model described in Ref. [28]. This model has two parameters which are fixed at the value $m = -0.38 \ln 2$ and $\sigma^2 = 0.03 \ln 2$. From the WT skeletons of 32 (1024×1024) images like the one in Figure 6a, one computes the average of the partition functions $\mathcal{Z}(q, a)$. As shown in Figure 7a, when plotted *versus* the scale parameter a in a logarithmic representation, these average partition functions display a rather impressive scaling behavior over a range of scales of about 4 octaves (*i.e.*, $\sigma_W \lesssim a \lesssim 16\sigma_W$, where $\sigma_W = 13$ pixels). Let us point out that scaling of quite good quality is found for a rather wide range of values of q: $-6 \lesssim q \lesssim 8$. When processing to a linear regression fit of
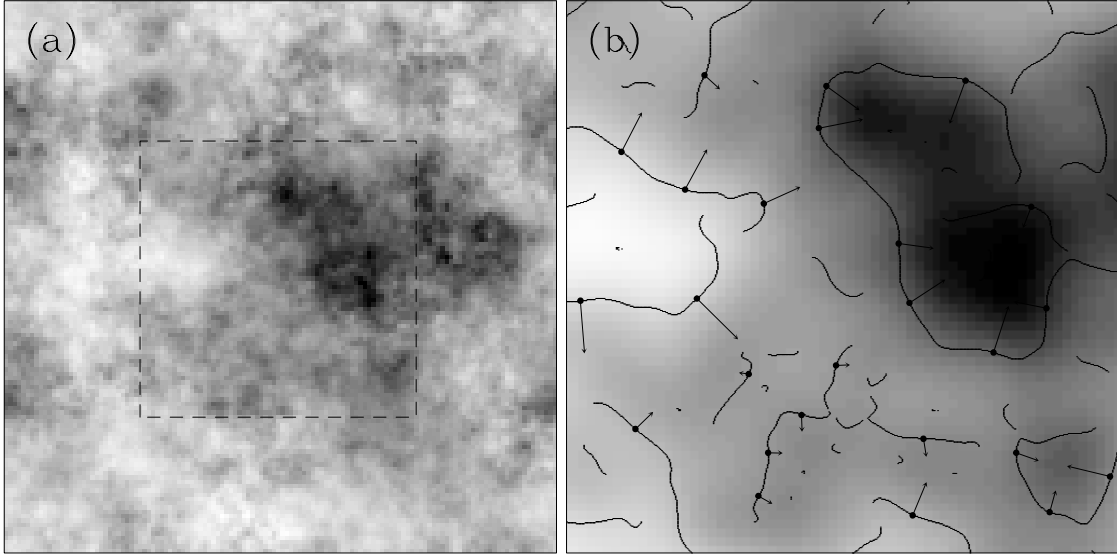
FIGURE 6. 2D wavelet transform analysis of a multifractal rough surface generated with the log-normal $\mathcal{W}$-cascade model with the parameter values $m = -0.38 \ln 2$ and $\sigma^2 = 0.03 \ln 2$ [28]. ψ is the first-order radially symmetric analyzing wavelet shown in Figure 1. (a) 32 grey-scale coding of the original (1024×1024) image. (b) Maxima chains and WTMMM for the central (512×512) part of the original image (dashed square in (a)) as computed at the scale $a = 2^{2.9} \sigma_W$. The smoothed image $\phi_{\mathbf{b},a} * f$ is shown as a grey-scale coded background from white (min) to black (max).

the data over the first four octaves, one gets the $\tau(q)$ spectrum ($\circ$) shown in Fig. 7b. For the range of q values where scaling is operating, the numerical data are in remarkable agreement with the theoretical nonlinear $\tau(q)$ spectrum [28] :

$$\tau(q) = -\frac{\sigma^2}{2 \ln 2} q^2 - \frac{m}{\ln 2} q - 2 \, . \tag{17}$$

Similar quantitative agreement is observed on the $D(h)$ singularity spectrum in Figure 7c which displays also a parabolic shape as predicted theoretically :

$$D(h) = -\frac{(h + m/\ln 2)^2}{2\sigma^2/\ln 2} + 2 \, . \tag{18}$$

The multifractal rough surfaces under study, display intermittent fluctuations corresponding to Hölder exponent values ranging from $h_{\min} = 0.034$ to $h_{\max} = 0.726$. Unfortunately, to capture the strongest and weakest singularities, one needs to compute the $\tau(q)$ spectrum for very large values of $|q|$. This requires the processing of many more images of much larger size, which is out of our current computer capabilities. Note that with the statistical sample studied here, one has $D(h(q=0) = 0.38) = 2.00 \pm 0.02$, which allows us to conclude that the rough surfaces under consideration are singular everywhere. The results reported in Figure 7 demonstrate that the 2D WTMM method is a very efficient tool to resolve multifractality.
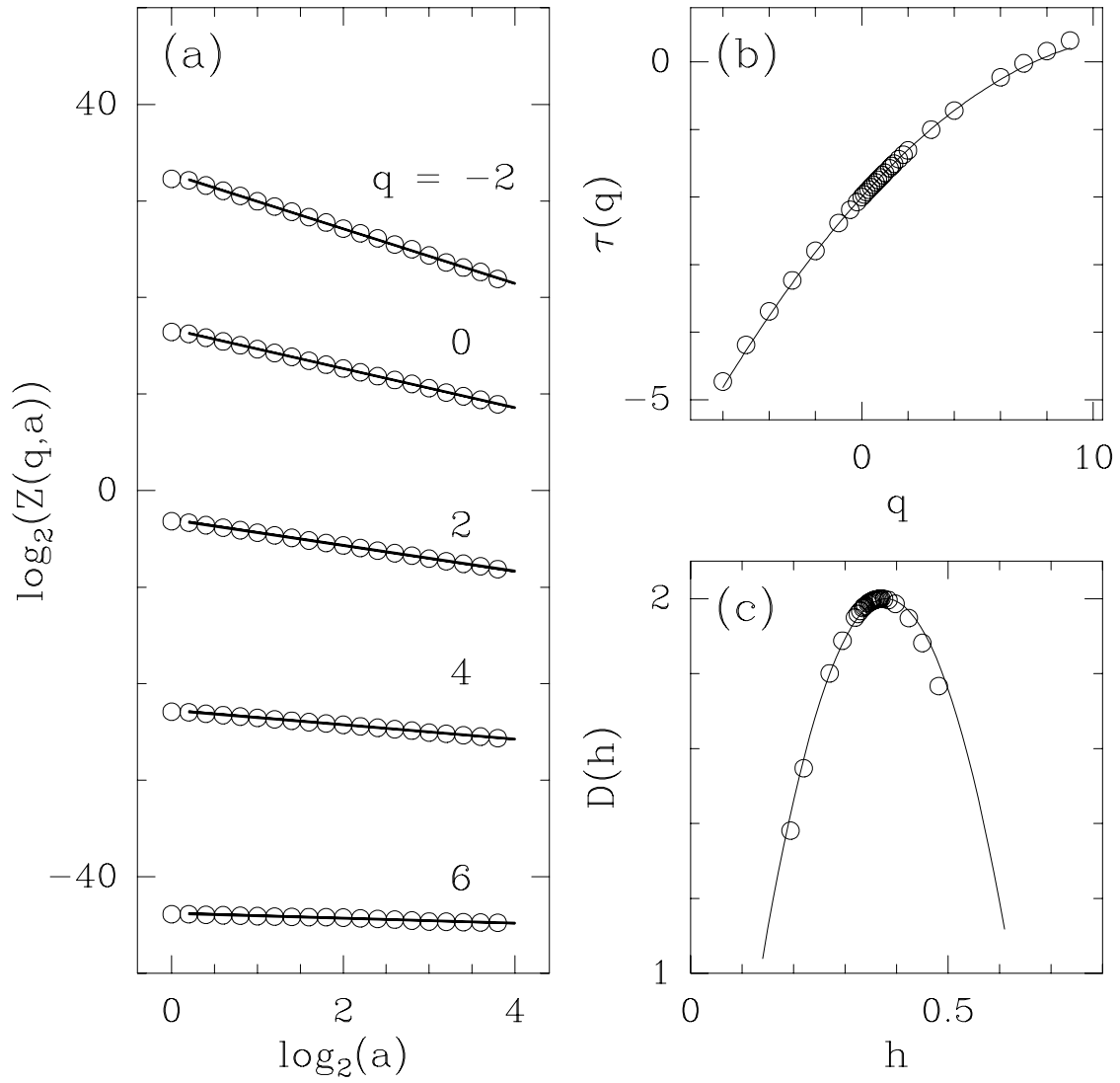
FIGURE 7. Determination of the $\tau(q)$ and $D(h)$ spectra of multifractal rough surfaces generated with the log-normal random $\mathcal{W}$-cascade models (○), using the 2D WTMM method [28]. ψ is the first-order radially symmetric analyzing wavelet used in Figure 6. (a) $\log_2 \mathcal{Z}(q,a)$ *vs* $\log_2 a$; the solid lines correspond to linear regression fit of the data over the first four octaves. (b) $\tau(q)$ *vs* q as obtained from linear regression fit of the data in (a) over the first four octaves. (c) $D(h)$ *vs* h, after Legendre transforming the $\tau(q)$ curve in (b). In (b) and (c), the solid lines represent the theoretical log-normal spectra (Eqs (17) and (18)).

APPLICATION OF THE 2D WTMM METHOD TO LANDSAT IMAGES OF STRATOCUMULUS CLOUDS

Landsat data of marine stratocumulus cloud scenes

Over the past fifteen years, Landsat imagery has provided the remote sensing community at large with a very attractive and reliable tool for studying the Earth's environment [9, 10, 11, 12, 13, 14, 15]. One of the main advantages of high-resolution satellite imagery is its rather low effective cost as compared to outfitting and flying research aircraft. Moreover, this very well calibrated instrument offers the possibility to reach unusual high spatial, spectral and radiometric resolutions [15]. Indeed, the five-channel Multi-Spectral Scanning (MSS, Landsat 1-3) radiometer resolves features down to 80 m with 7 bits of dynamic range. The seven-channel Thematic Mapper (TM, Landsat 4-5) camera does even better with a resolution of 30 m and a dynamic range of 8 bits. Both these instruments are essentially proportional to nadir-viewing radiance at satellite level ($\simeq 800$ km). Scores of Landsat completely or partially cloudy scenes have thus been acquired, mainly for the purpose of characterizing cloud morphology. Mainly two types of statistical analysis have been applied so far to Landsat imagery: spectral analysis of the 2D radiance field [12, 13, 14, 15, 47] and joint area and perimeter distributions for ensembles of individual clouds [9, 10, 11] defined by some threshold in radiance. One of the most remarkable properties of Landsat cloud scenes is their statistical "scale-invariance" over a rather large range of scales, which justifies why fractal and multifractal concepts have progressively gained more acceptance in the atmospheric scientist community [4].

Off all cloud types, marine stratocumulus (Sc) are without any doubt the ones which have attracted the most attention, mainly because of their first-order effect on the Earth's energy balance [4, 15, 47]. Being at once very persistent and horizontally extended, marine Sc layers carry considerable weight in the overall reflectance (albedo) of the planet and, from there, command a strong effect on its global climate [5]. Furthermore, with respect to climate modeling [6] and the major problem of cloud-radiation interaction [13, 15, 48, 49], they are presumably at their simplest in marine Sc which are relatively thin (~ 300-500 m), with well-defined (quasi-planar) top and bottom, thus approximating the plane-parallel geometry where radiative transfer theory is well developed [15, 48, 49, 50]. However, because of its internal homogeneity assumption, plane-parallel theory shows systematic biases due to the huge internal variability of marine Sc [8, 26].

Figure 8 is a grey-scale rendering of a small part of the entire ($\simeq 196 \times 168$ km^2) original cloudy Landsat 5 scene captured with the TM camera (1 pixel $= 30$ m) in the 0.6-0.7 μm channel (*i.e.* reflected solar photons as opposed to their counterparts emitted in the thermal infrared) during the first ISCCP (International Satellite Cloud Climatology Project) Research Experiment (FIRE) field program [51], which took place over the Pacific Ocean off San Diego in summer 1987. In order to master edge effects in the 2D WT computation, we actually select 32 overlapping 1024×1024 pixels^2 subscenes in this cloudy region. The overall extend of the explored area is about 7840 km^2. Figure 8a shows a typical (1024×1024) portion of the original image where the eight-bit grey scale coding of the quasi-nadir viewing radiance clearly reveals the presence of some
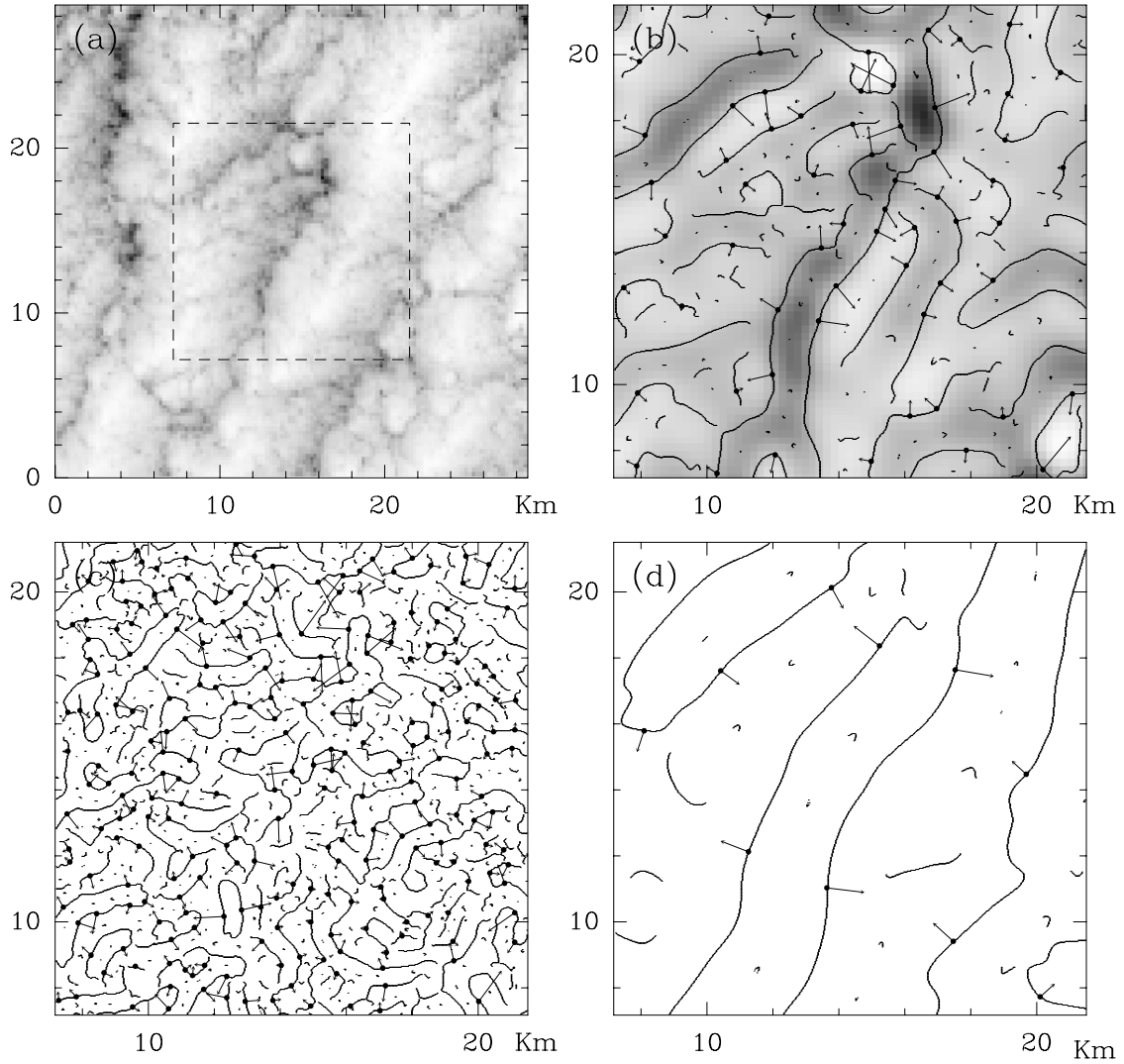
FIGURE 8. 2D wavelet transform analysis of a Landsat image of marine Sc clouds [31]. $\psi(\mathbf{x})$ is the first-order radially symmetric analyzing wavelet shown in Figure 1. (a) 256 grey-scale coding of a (1024×1024) portion of the original radiance image. In (b) $a = 2^{2.9}\sigma_W$, (c) $a = 2^{1.9}\sigma_W$ and (d) $a = 2^{3.9}\sigma_W$ (where $\sigma_W = 13$ pixels $\simeq 390$ m), are shown the maxima chains; the local maxima of $\mathcal{M}_\psi$ along these chains are indicated by ($\bullet$) from which originates an arrow whose length is proportional to $\mathcal{M}_\psi$ and its direction (with respect to the x-axis) is given by $\mathcal{A}_\psi$; only the central (512×512) part delimited by a dashed square in (a) is taken into account to define the WT skeleton. In (b), the smoothed image $\phi_{\mathbf{b},a} * I$ is shown as a grey-scale coded background from white (min) to black (max).

anisotropic texture induced by convective structures which are generally aligned to the wind direction.

The computation of the power spectral density reveals a rather nice power-law behavior $S(k) \sim k^{-\beta}$ from $0.2 - 0.4$km up to $\simeq 6$km, with $\beta = 2.72 \pm 0.08$. This value of the spectral exponent is quite compatible with previous estimates obtained for 1D LWC data [7, 12, 13, 14, 15, 47], namely $\beta_{LWC} = 1.4$-$1.7 \simeq \beta_{2D} - 1$.

Numerical computation of the multifractal $\tau(q)$ and $D(h)$ spectra using the 2D WTMM method

In Figure 8 is illustrated the computation of the maxima chains and the WTMMM for the studied marine Sc [31] scene. In Figure 8b is shown the convolution of the original radiance field (Fig. 8a) with the isotropic gaussian smoothing filter ϕ (Eq. (2)). According to the definition of the WTMM, the maxima chains correspond to well defined edge curves of the smoothed image. The local maxima of $\mathcal{M}_\psi$ along these curves are indicated by ($\bullet$) from which originates an arrow whose length is proportional to $\mathcal{M}_\psi$ and its direction (with respect to the x-axis) is given by $\mathcal{A}_\psi$. After linking these WTMMM across scales, one constructs the WT skeleton from which one computes the partition functions $\mathcal{Z}(q,a)$ (Eq. (12)). As reported in Figure 9a, the partition functions averaged over the 32 overlapping (1024×1024) images ($\bullet$), display some well-defined scaling behavior over the first three octaves, *i.e.* over the range of scales $390 \text{ m} \lesssim a \lesssim 3120 \text{ m}$, when plotted *versus* a in a logarithmic representation. Indeed the scaling deteriorates progressively from the large scale side when one goes to large values of $|q| \gtrsim 3$. As reported in Ref. [31], besides the fact that we are suffering from insufficient sampling, the presence of localized Dirac like structures is likely to explain the fact that the observed cross-over to a steeper power-law decay occurs at a smaller and a smaller scale when one increases $q > 0$. Actually for $q \gtrsim 3$, the cross-over scale $a^* \lesssim 1200 \text{ m}$ becomes significantly smaller than the so-called integral scale which is approximately given by the characteristic width $\lambda \simeq 5\text{-}6 \text{ km}$ of the convective rolls (Fig. 8a). When processing to a linear regression fit of the data in Figure 9a over the first octave and a half (in order to avoid any bias induced by the presence of the observed cross-over at large scales), one gets the $\tau(q)$ spectrum ($\bullet$) shown in Figure 9b. In contrast to the previously studied fractional Brownian rough surfaces, this $\tau(q)$ spectrum unambiguously deviates from a straight line. When Legendre transforming this nonlinear $\tau(q)$ curve, one gets the $D(h)$ singularity spectrum reported in Figure 9c. Its characteristic single humped shape over a finite range of Hölder exponents is a clear signature of the multifractal nature of the marine Sc radiance fluctuations.

In Figure 9 are also shown for comparison the results ($\circ$) obtained when applying the 2D WTMM method with a third-order ($n_\psi = 3$) radially symmetric analyzing wavelet (the smoothing function ϕ being the isotropic 2D mexican hat). As seen in Figure 9a, the use of a wavelet which has more zero moments seems to slightly improve scaling. But the estimate of the $\tau(q)$ and $D(h)$ spectra yields consistent results in the range $-3 \lesssim q \lesssim 5$. Moreover these spectra are very well fitted by the theoretical quadratic spectra (Eqs (17) and (18)) predicted for log-normal $\mathcal{W}$-cascades [31].

WTMMM probability density functions

In Figures 10a and 10b are respectively shown the pdf's $P_a(\mathcal{M})$ and $P_a(\mathcal{A})$ for three different values of the scale parameter $a = 2^{0.3}\sigma_W$ (480 m), $2^{1.3}\sigma_W$ (960 m) and $2^{2.3}\sigma_W$ (1920 m). First let us concentrate on the results shown in Figure 10b for $P_a(\mathcal{A})$. This distribution is clearly scale dependent with some evidence of anisotropy enhancement
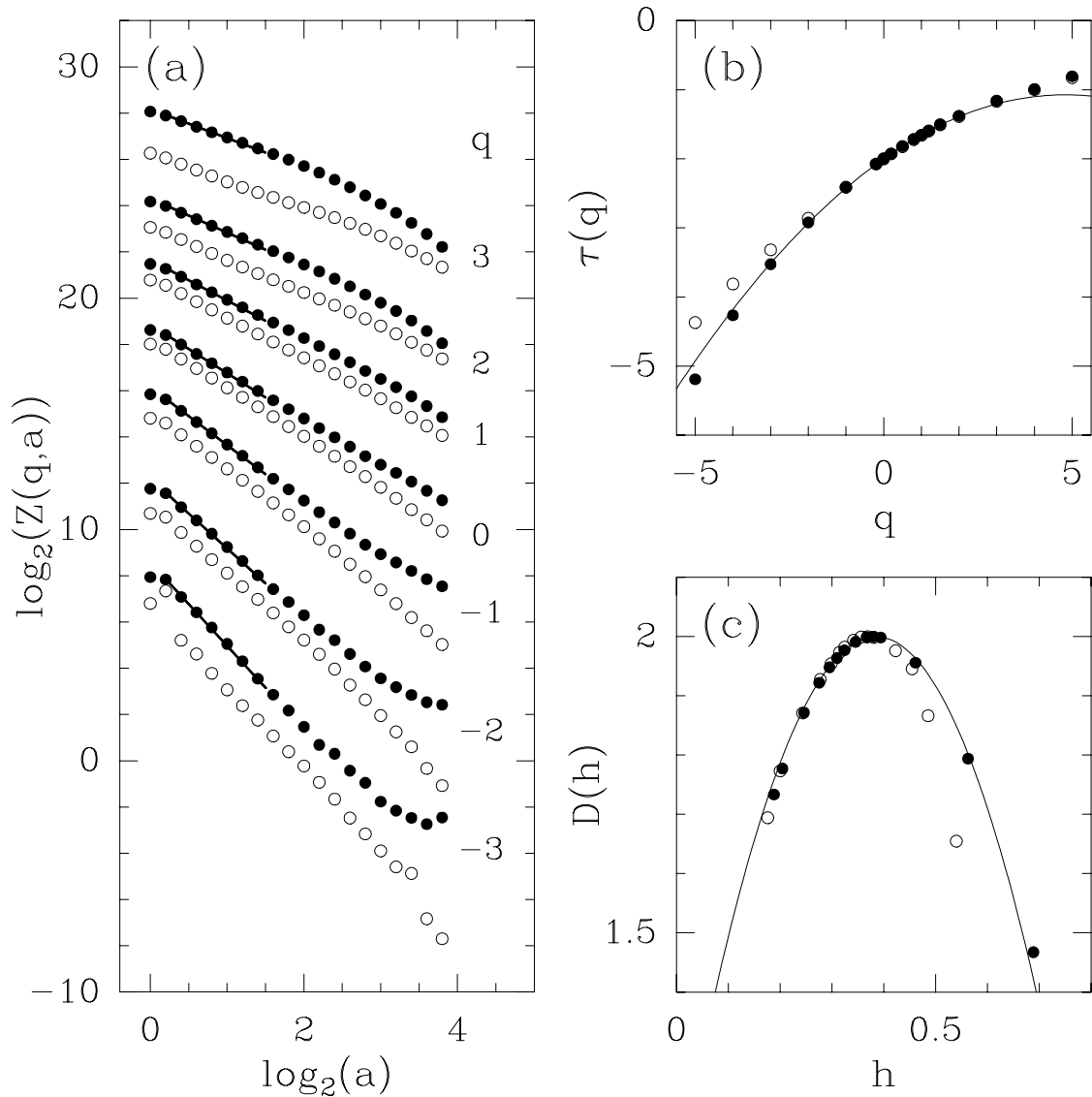
FIGURE 9. Determination of the $\tau(q)$ and $D(h)$ spectra of radiance Landsat images of marine Sc [31]. The 2D WTMM method is used with either a first-order (●) or a third-order (○) radially symmetric analyzing wavelet (see Fig. 1). (a) $\log_2 \mathcal{Z}(q,a)$ *vs* $\log_2 a$; the solid lines correspond to linear regression fits of the data over the first and a half octave. (b) $\tau(q)$ *vs* q as obtained from a linear regression fit of the data in (a). (c) $D(h)$ *vs* h, after Legendre transforming the $\tau(q)$ curve in (b). In (b) and (c), the solid lines correspond to the theoretical multifractal spectra for log-normal $\mathcal{W}$-cascades with parameter values $m = -0.38 \ln 2$ and $\sigma^2 = 0.07 \ln 2$ (Eqs (17) and (18)).

when going from small to large scales, in particular when one reaches scales which become comparable to the characteristic width of the convective structures (*i.e.*, a few kilometers wide). Two peaks around the values $\mathcal{A} \simeq -\pi/6$ and $5\pi/6$ become more and more pronounced as the signature of a privilegied direction in the analyzed images. As one can check from a visual inspection of Figure 8a, this direction is nothing but the perpendicular to the mean direction of the convective rolls that are generally aligned to
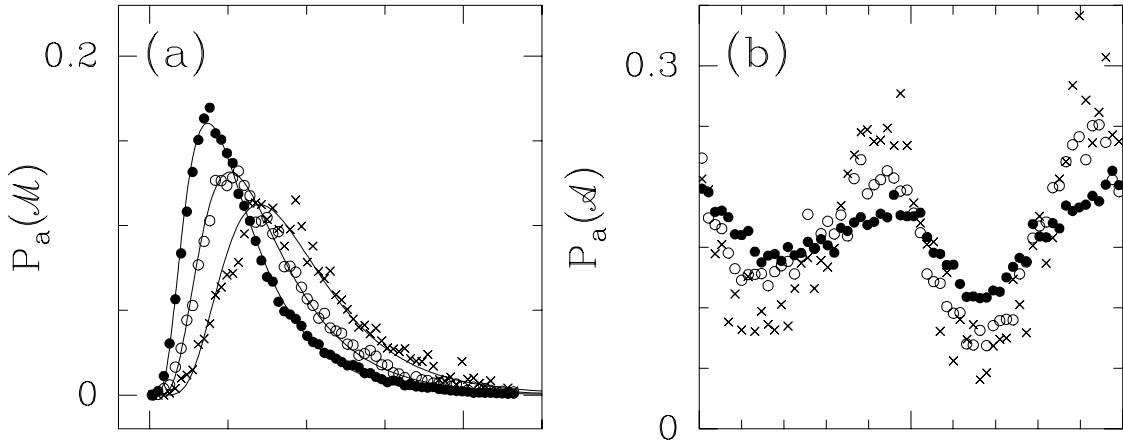
FIGURE 10. Pdf's of the WTMMM coefficients of the 32 (1024×1024) radiance Landsat images as computed with a first-order radially symmetric analyzing wavelet: (a) $P_a(\mathcal{M})$ *vs* $\mathcal{M}$; (b) $P_a(\mathcal{A})$ *vs* $\mathcal{A}$; the symbols correspond to the following scales $a = 2^{0.3}\sigma_W = 480$ m ($\bullet$), $2^{1.3}\sigma_W = 960$ m ($\circ$) and $2^{2.3}\sigma_W = 1920$ m ($\times$).

the wind direction.

However, as seen in Figure 11, when conditioning the pdf of $\mathcal{M}$ by the argument $\mathcal{A}$, the shape of this pdf turns out to be independent of the considered value of $\mathcal{A}$, as long as the value of the scale parameter a remains small as compared to the characteristic width of the convective structures. The observation that the joint probability distribution actually factorizes, *i.e.*, $P_a(\mathcal{M}, \mathcal{A}) = P_a(\mathcal{M})P_a(\mathcal{A})$, is the signature that $\mathcal{M}$ and $\mathcal{A}$ are likely to be independent [30, 31]. This actual decoupling of $\mathcal{M}$ and $\mathcal{A}$ means that the multifractal properties of the marine Sc radiance fluctuations are contained in the way the shape of the pdf of $\mathcal{M}$ evolves when one decreases the scale parameter a. In other words the anisotropy induced by the wind direction does not affect the multifractal scaling properties of the cloud structure.

DISCUSSION

To summarize, we have reported the results of the experimental application of the 2D WTMM method [20, 28] to radiance Landsat images of marine Sc clouds collected during FIRE program [30, 31]. The computation of the $\tau(q)$ and $D(h)$ spectra have definitely quantified the multifractal scaling properties of the radiance fields. Besides the presence of rather isolated localized downward spike events [31], the internal cloud structure is clearly intermittent and displays rather convincing isotropic scaling over a range of scale that extends from our WT microscope resolution ($\sigma_W = 13$ pixels $= 390$ m) up to $L/2$, where $L \sim 5$-6 km is some integral scale which is apparently dictated by the average characteristic width of the convective rolls that modulate the amplitude of radiance fluctuations.

Let us point out that a similar 1D WTMM analysis of the velocity fluctuations in high Reynolds number turbulence has come to conclusions very close to those of the present study [52, 53]. Besides the presence of rather localized Dirac like structures that witness
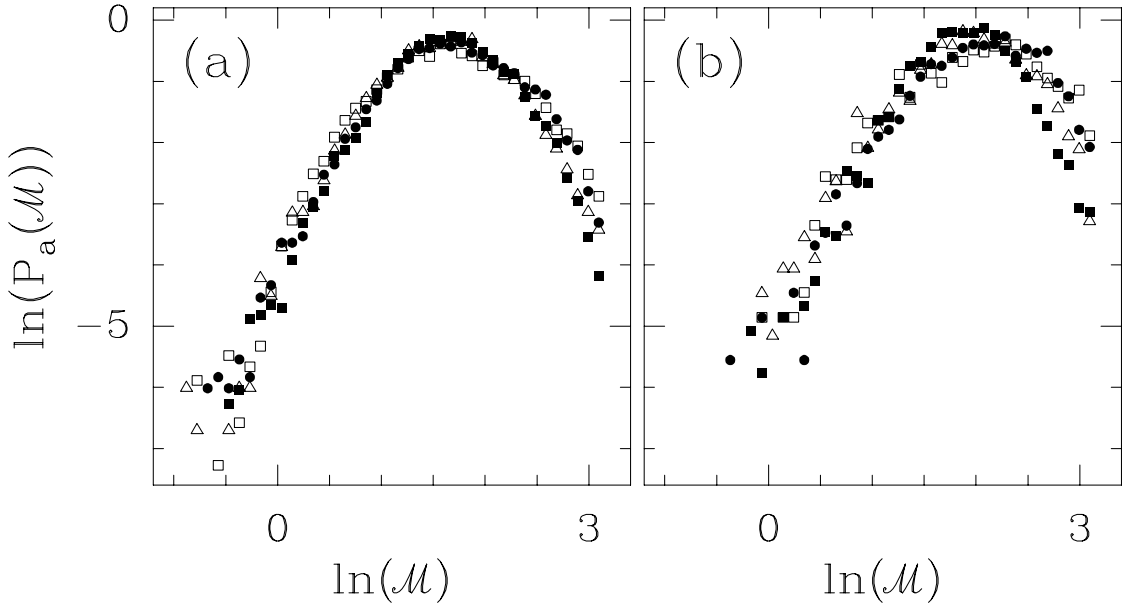
FIGURE 11. Pdf's of the WTMMM coefficients of the 32 (1024 × 1024) radiance Landsat images as computed with a first-order radially symmetric analyzing wavelet. Pdf's of $\mathcal{M}$ when conditioned by $\mathcal{A}$. The different symbols correspond to fixing $\mathcal{A}$ (mod π) to $0 \pm \pi/8$ (○), $\pi/4 \pm \pi/8$ (□), $\pi/2 \pm \pi/8$ (△) and $3\pi/4 \pm \pi/8$ (■). (a) $a = 2^{0.3}\sigma_W = 480$ m; (b) $a = 2^{1.3}\sigma_W = 960$ m.

to the probing of vorticity filaments [54], the multifractal nature of turbulent velocity is likely to be understood in terms of a log-normal cascading process which is expected to be scale-invariant in the limit of very high Reynolds numbers [52, 53]. In Figure 12 are shown for comparison the results obtained in Figure 9 for the $D(h)$ singularity spectrum of the radiance Landsat images together with the $D(h)$ data extracted from the 1D analysis of a turbulent velocity signal recorded at the Modane wind tunnel ($R_\lambda \simeq 2000$) [52, 53] (indeed $D(h) + 1$ is represented for the latter in order to compare 1D to 2D data). The turbulent velocity $D(h)$ spectrum significantly differs from the results obtained for the marine Sc cloud. They have a common feature, *i.e.*, the Hölder exponent the most frequently encountered in the radiance field $h = m/\ln 2 = h(q = 0) = \partial\tau/\partial q|_{q=0} = 0.38 \pm 0.01$ is undistinguishable from the corresponding exponent $h = h(q = 0) = 0.39 \pm 0.01$ found for the turbulent velocity field. Note that these values are significantly larger than the theoretical value $h = 1/3$ predicted by Kolmogorov in 1941 [55] to account for the observed $k^{-5/3}$ power-spectrum behavior. The main difference comes from the intermittency parameter which is much stronger for the cloud, $\sigma^2/\ln 2 = 0.08 \pm 0.01$ ($n_\psi = 1$) or $\sigma^2/\ln 2 = 0.06 \pm 0.01$ ($n_\psi = 3$) than for the turbulent velocity, $\sigma^2/\ln 2 = 0.036 \pm 0.004$. This is the signature that the radiance field is much more intermittent than the velocity field: the $D(h)$ singularity spectrum for the former is unambiguously wider than the corresponding spectrum for the later. (Let us mention that insufficient sampling is probably at the origin of the underestimation of the intermittency parameter $c_2 = \sigma^2/\ln 2$ when using a third-order analyzing wavelet. This means that one must not pay too much attention to the decreasing right-hand part of the $D(h)$ cloud data in Figure 12b.) For the sake of comparison, we have also reported in Figure 12,
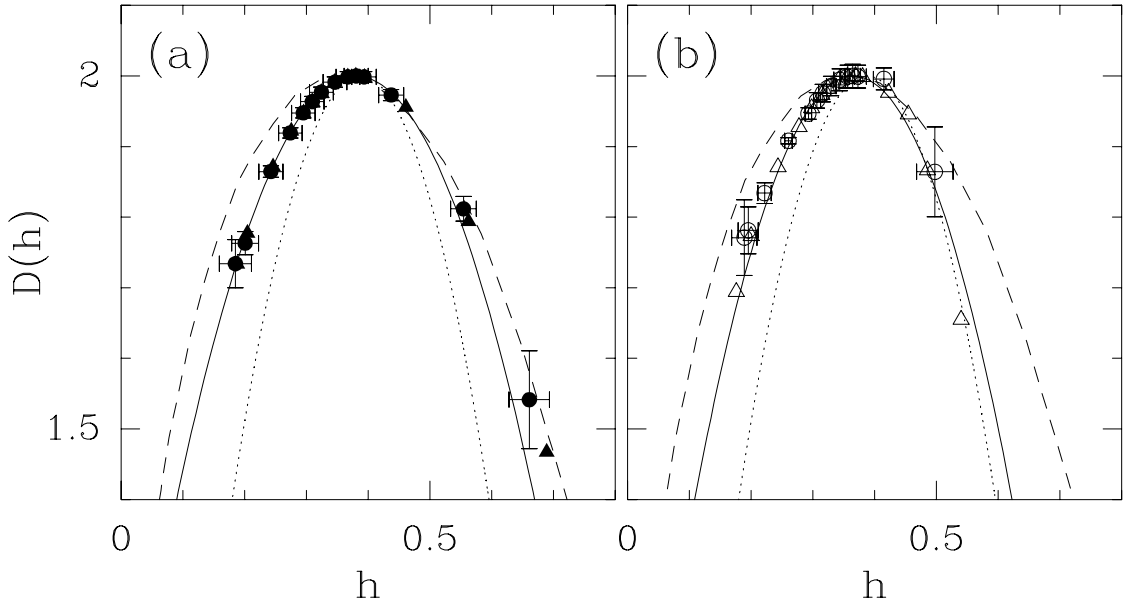
FIGURE 12. $D(h)$ singularity spectrum of the radiance Landsat images as computed with the 2D WTMM method using a first-order (a) or a third-order (b) radially symmetric analyzing wavelet. Same computations as in Figures 9c. The solid lines correspond to the log-normal quadratic spectrum with $m = -0.38\ln 2, \sigma^2 = 0.08\ln 2$ (a) and $m = -0.366\ln 2, \sigma^2 = 0.06\ln 2$ (b). The $D(h)$ singularity spectrum of velocity (dotted lines) and temperature (dashed lines) fluctuations in fully developed turbulence are shown for comparison.

the multifractal $D(h)$ spectrum of the temperature fluctuations recorded in a $R_\lambda = 400$ turbulent flow [56]. The corresponding single humped curve is definitely much wider than the velocity $D(h)$ spectrum and it is rather close to the data corresponding to the marine Sc radiance field. It is well recognized however that liquid water is not really passive and that its identification with a passive component in atmospheric dynamics offers limited insight into cloud structure since, by definition, near-saturation conditions prevail and latent heat production affects buoyancy. So cloud microphysical processes are expected to interact with the circulation at some, if not all, scales [57]. Nevertheless, our results in Figure 12 tell us that from a multifractal point of view, the intermittency captured by the Landsat satellite looks statistically equivalent to the intermittency of a passive scalar in fully-developed 3D turbulence. The fact that the internal structure of Sc cloud somehow reflects some statistical properties of atmospheric turbulence is not such a surprise in this highly turbulent environment.

Finally, with respect to the issue of cloud modeling, it comes out quite naturally from the WTMM analysis of marine Sc Landsat data, that the 2D random $\mathcal{W}$-cascade models introduced in Ref. [28], are much more realistic hierarchical models than commonly used multifractal models like the fractionally integrated singular cascade [22, 25, 47] or the bounded cascade models [58]. We are quite optimistic in view of using the log-normal $\mathcal{W}$-cascade models with realistic parameter values for radiation transfer simulations. To our opinion, random $\mathcal{W}$-cascade models are a real breakthrough, not only for the general purpose of image synthesis, but more specifically for cloud modeling. It

is likely that better cloud modeling will make further progress in our understanding of cloud-radiation interaction possible.

ACKNOWLEDGMENTS

REFERENCES

1. Monin, A. S., and Yaglom, A. M., *Statistical Fluid Mechanics*, vol. 2, MIT Press, Cambridge, MA, 1975.
2. Frisch, U., *Turbulence*, Cambridge Univ. Press, Cambridge, 1995.
3. Lovejoy, S., *Science*, **216**, 185 (1982).
4. Wilkinson, G. G., Kanellopoulos, J., and Megier, J., editors, *Fractals in Geoscience and Remote Sensing*, Image Understanding Research Series, vol.1, ECSC-EC-EAEC, Brussels, Luxemburg, 1995.
5. Ramanatahn, V., Cess, R. D., Harrison, E. F., Minnis, P., Barkston, B. R., Ahmad, E., and Hartmann, D., *Science*, **243**, 57 (1989).
6. Cess, R. D., et al., *Science*, **245**, 513 (1989).
7. Davis, A., Marshak, A., Wiscombe, W. J., and Cahalan, R. F., *J. Atmos. Sci.*, **53**, 1538 (1996).
8. Marshak, A., Davis, A., Wiscombe, W. J., and Cahalan, R. F., *J. Atmos. Sci.*, **54**, 1423 (1997).
9. Welch, R. M., Kuo, K. S., Wielicki, B. A., Sengupta, S. K., and Parker, L., *J. Appl. Meteor.*, **27**, 341 (1988).
10. Cahalan, R. F., and Joseph, J. H., *Mon. Wea. Rev.*, **117**, 261 (1989).
11. Sèze, G., and Smith, L., "", in *Proc. Seventh Conf. on Atmospheric Radiation, Amer. Meteor. Soc., San Francisco, CA*, 1990, p. 47.
12. Cahalan, R. F., and Snider, J. B., *Remote Sens. Environ.*, **28**, 95 (1989).
13. Baker, H. W., and Davies, J. A., *Remote Sens. Environ.*, **42**, 51 (1992).
14. Lovejoy, S., Schertzer, D., Silas, P., Tessier, Y., and Lavallée, D., *Ann. Geophysicae*, **11**, 119 (1993).
15. Davis, A., Marshak, A., Cahalan, R. F., and Wiscombe, W. J., *J. Atmos. Sci.*, **54**, 241 (1997).
16. Mandelbrot, B. B., *Fractals : Form, Chance and Dimensions*, Freeman, San Francisco, 1977; *The Fractal Geometry of Nature*, Freeman, San Francisco, 1982.
17. Corssin, S., *J. Appl. Phys.*, **22**, 469 (1951).
18. Obukhov, A., *Izv. Akad. Naut. SSSR, Ser. Geogr. I. Geofiz.*, **13**, 55 (1949).
19. Kraichnan, R. H., *Phys. Fluids*, **10**, 1417 (1967).
20. Arneodo, A., Decoster, N., and Roux, S. G., *Eur. Phys. J. B*, **15**, 567 (2000).
21. Schertzer, D., and Lovejoy, S., *Phys. Chem. Hyd. J.*, **6**, 623 (1985).
22. Schertzer, D., and Lovejoy, S., *J. Geophys. Res.*, **92**, 9693 (1987).
23. Schertzer, D., and Lovejoy, S., *Fractals in Geoscience and Remote Sensing*, p. 11, vol. 1 of [4] (1995).
24. Lovejoy, S., and Schertzer, D., *Fractals in Geoscience and Remote Sensing*, p. 102, vol. 1 of [4] (1995).
25. Schertzer, D., Lovejoy, S., Schmitt, F., Ghigisinskaya, Y., and Marsan, D., *Fractals*, **5**, 427 (1997).
26. Davis, A., Marshak, A., Wiscombe, W. J., and Cahalan, R. F., *J. Geophys. Res.*, **99**, 8055 (1994).
27. Wiscombe, W. J., Davis, A., Marshak, A., and Cahalan, R. F., in *Proc. of the Fourth Atmospheric Radiation Measurement (ARM) Science Team Meeting, Charleston, U.S. Dept. of Energy*, 1995, p. 11.
28. Decoster, N., Roux, S. G., and Arneodo, A., *Eur. Phys. J. B*, **15**, 739 (2000).

29. Arrault, J., Arneodo, A., Davis, A., and Marshak, A., *Phys. Rev. Lett.*, **79**, 75 (1997).
30. Arneodo, A., Decoster, N., and Roux, S. G., *Phys. Rev. Lett.*, **83**, 1255 (1999).
31. Roux, S. G., Arneodo, A., and Decoster, N., *Eur. Phys. J. B*, **15**, 765 (2000).
32. Muzy, J. F., Bacry, E., and Arneodo, A., *Phys. Rev. E*, **47**, 875 (1993).
33. Meyer, Y., and Roques, S., editors, *Progress in Wavelets Analysis and Applications*, Editions frontières, Gif-sur-Yvette, 1993.
34. Mallat, S., *A Wavelet Tour in Signal Processing*, Academic Press, New York, 1998.
35. Marr, D., *Vision*, W. H. Freemann and Co, San-Francisco, 1982.
36. Mallat, S., and Zhong, S., *IEEE Trans. on Pattern Analysis and Machine Intelligence*, **14**, 710 (1992).
37. Mallat, S., and Hwang, W. L., *IEEE Trans. on Information Theory*, **38**, 617 (1992).
38. Canny, J., *IEEE Trans. Patt. Anal. Machine Intell.*, **8**, 679 (1986).
39. Farmer, J. D., Ott, E., and Yorke, J. A., *Physica D*, **7**, 153 (1983).
40. Argoul, F., Arneodo, A., Elezgaray, J., Grasseau, G., and Murenzi, R., *Phys. Rev. A*, **41**, 5537 (1990).
41. Muzy, J. F., Bacry, E., and Arneodo, A., *Phys. Rev. Lett.*, **67**, 3515 (1991).
42. Muzy, J. F., Bacry, E., and Arneodo, A., *Int. J. of Bifurcation and Chaos*, **4**, 245 (1994).
43. Arneodo, A., Bacry, E., and Muzy, J. F., *Physica A*, **213**, 232 (1995).
44. Mandelbrot, B. B., and Van Ness, J. W., *S.I.A.M. Rev.*, **10**, 422 (1968).
45. Peitgen, H. O., and Saupe, D., editors, *The Science of Fractal Images*, Springer Verlag, New York, 1987.
46. Lévy, P., *Processus Stochastiques et Mouvement Brownien*, Gauthier-Villars, Paris, 1965.
47. Davis, A., Marshak, A., Wiscombe, W. J., and Cahalan, R. F., *Topics in Nonstationary Analysis*, World Scientific, Singapore, 1996, p. 97.
48. Davis, A., Lovejoy, S., and Schertzer, D., *Scaling, Fractals and Nonlinear Variability in Geophysics*, Kluwer, Dordrecht, 1991, p. 303.
49. Cahalan, R. F., Ridgway, W., Wiscombe, W. J., Gollmer, S., and Harshvardan, M., *J. Atmos. Sci*, **51**, 3776 (1994).
50. Cahalan, R. F., *Advances in Remote Sensing and Retrieval Methods*, Deepak Pub, Hampton, 1989, p. 371.
51. Cox, S., McDougal, D., Randall, D., and Schiffer, R., *Bull. Amer. Meteor. Soc.*, **68**, 114 (1987).
52. Arneodo, A., Manneville, S., and Muzy, J. F., *Eur. Phys. J. B*, **1**, 129 (1998).
53. Arneodo, A., Manneville, S., Muzy, J. F., and Roux, S. G., *Phil. Trans. R. Soc. London A*, **357**, 2415 (1999).
54. Roux, S. G., Muzy, J. F., and Arneodo, A., *Eur. Phys. J. B*, **8**, 301 (1999).
55. Kolmogorov, A. N., *C. R. Acad. Sci. USSR*, **30**, 301 (1941).
56. Ruiz-Chavarria, G., Baudet, C., and Ciliberto, S., *Physica D*, **99**, 369 (1996).
57. Meong, C. H., Cotton, W. R., Bretherton, C., Chlond, A., Khairoutdinov, M., Krueger, S., Lewellen, W. S., McVean, M. K., Pasquier, J. R. M., Rand, H. A., Siebesma, A. P., Stevens, B., and Sykes, R. I., *Bull. Am. Meteor. Soc.*, **77**, 261 (1996).
58. Marshak, A., Davis, A., Cahalan, R. F., and Wiscombe, W. J., *Phys. Rev. E*, **49**, 55 (1994).